Research Square

Preprints are preliminary reports that have not undergone peer review.
They should not be considered conclusive, used to inform clinical practice,
or referenced by the media as validated information.

LRRK2 G2019S links myeloperoxidase-dependent neutrophil extracellular traps to enteric α- synuclein through RAB10 phosphorylation

Yuan-Kai Cheng
National Taiwan University
Kai-Quan Leong
National Taiwan University
Pei-Jie Lin
National Taiwan University
Mu-Jou Chen
National Taiwan University
Chih-Ying Lin
National Taiwan University
Yu-Wen Hsiao
National Taiwan University
Jou-Min Wang
National Taiwan University
Si-Lu Ma
National Taiwan University
Yi-He Lin
National Taiwan University
Ju-Pei Su
National Taiwan University
Hsin-An Shih
Academia Sinica
Ching-Wen Cheng
Academia Sinica
Huan-Yuan Chen
Academia Sinica
Steven Lin
Academia Sinica
Chin-Hsien Lin
National Taiwan University Hospital

Hao-Sen Chiang

hschiang@ntu.edu.tw

National Taiwan University

Article

Keywords:

Posted Date: November 26th, 2026

DOI: https://doi.org/10.21203/rs.3.rs-11793112/v1

License: This work is licensed under a Creative Commons Attribution 4.0 International License.
Read Full License

Additional Declarations: No competing interests reported.

Abstract

LRRK2 is a risk gene shared by Parkinson's disease and inflammatory bowel disease and is expressed in neutrophils, but how the G2019S variant alters neutrophil effector function in the inflamed gut is unclear. During acute dextran sulfate sodium–induced colitis, G2019S mice formed more colonic neutrophil extracellular traps (NETs) than non-transgenic littermates despite comparable neutrophil numbers and disease severity; after repeated colitis they developed more severe disease with colonic α-synuclein accumulation. DNase I and PAD4 deficiency each partially attenuated colitis and lowered colonic α-synuclein, and colonic NETs were nearly absent in germ-free mice. Ionomycin-stimulated G2019S neutrophils showed increased RAB10 Thr73 phosphorylation and released more NETs in a kinase-dependent manner. Phosphomimetic RAB10 was sufficient to enhance NET release, and myeloperoxidase inhibition or hypochlorous acid scavenging selectively abolished the enhanced response. These findings implicate RAB10 and myeloperoxidase in LRRK2-driven NET formation and link this response to enteric α-synuclein accumulation.

Introduction

Parkinson's disease (PD) is increasingly viewed as a systemic disorder in which gastrointestinal abnormalities may precede or accompany neurological manifestations[1,2]. In the body-first model of PD, α-synuclein pathology is proposed to arise in the enteric nervous system and to spread rostrally along the vagus nerve[1,2], and the epidemiological observation that truncal vagotomy is associated with a reduced long-term risk of PD is consistent with this route[3]. In keeping with an intestinal contribution to disease-relevant pathology, patients with PD exhibit intestinal α-synuclein accumulation[4,5], elevated colonic inflammatory cytokines[6], and altered gut microbiota[7]. Experimental inoculation of the gut wall with α-synuclein preformed fibrils[8] and intestinal infection[9] can promote brain pathology and PD-like phenotypes in animal models. In parallel, patients with inflammatory bowel disease (IBD) have an increased risk of developing PD[10,11], and anti-tumor necrosis factor therapy is associated with a lower incidence of PD in this population[11]. Together, these observations position chronic intestinal inflammation as an accessible and potentially modifiable component of the gut–brain axis in PD. The immune effector mechanisms that translate PD-associated genetic risk into gut pathology, however, remain insufficiently defined.

Leucine-rich repeat kinase 2 (LRRK2) is one of the most important genetic risk factors for PD. LRRK2 is a multidomain kinase, and hyperactive LRRK2 variants are associated with increased PD risk[12]. LRRK2 regulates several cellular pathways relevant to neuronal and immune function, including endosomal trafficking[13], autophagy[14,15], and mitophagy[16]. In neuronal systems, PD-associated LRRK2 variants alter neuronal morphology and activity[17,18], promote neurodegenerative phenotypes[19,20], and facilitate α-synuclein pathology[21]. These findings establish LRRK2 kinase activity as a central component of PD pathogenesis.

LRRK2 also has prominent functions outside the nervous system. It is highly expressed in immune-related tissues[22], and genetic links between LRRK2 and leprosy susceptibility support an immune-associated role for this kinase[23,24]. LRRK2 regulates multiple innate immune processes, including phagocytosis[25], NLRC4 inflammasome activation[26], proinflammatory cytokine production[27,28], and necroptosis[29]. Importantly, LRRK2 has also been identified as a shared risk locus for IBD and PD[30,31]. However, mouse colitis studies have reached different conclusions about whether LRRK2 promotes or restrains intestinal inflammation[27,32], suggesting that cell type, inflammatory context, and upstream microbial cues may determine its effects. This uncertainty is particularly relevant for neutrophils, which express high levels of LRRK2 but remain relatively understudied compared with macrophages and neurons. Two recent studies bear directly on this question. In a chronic dextran sulfate sodium (DSS) model, LRRK2 G2019S knock-in mice showed an exacerbated colitis phenotype that was fully rescued by transplantation of wild-type bone marrow, establishing that mutant LRRK2 acts through immune cells in chemically induced colitis[33]. In infectious colitis, LRRK2 G2019S enhanced neutrophil chemotaxis and NET formation in a kinase-dependent manner[34]. Which neutrophil effector program is engaged, and through which LRRK2 substrate, has not been defined in either setting.

Neutrophils shape inflammation in part through neutrophil extracellular traps (NETs), extruded networks of decondensed chromatin decorated with granule proteins such as myeloperoxidase (MPO) and neutrophil elastase (NE). NETs amplify mucosal injury in IBD[35] and have been implicated across a range of central nervous system (CNS) pathologies, including neurodegenerative disease, where NET components can injure the neurovascular unit and sustain neuroinflammation[36]. Because NET release deposits extracellular chromatin, histones, and oxidant-generating enzymes into the surrounding tissue, it offers a plausible route by which hyperactive kinase signaling in peripheral neutrophils could remodel the inflammatory environment of the gut and, in turn, PD-relevant enteric pathology. Whether pathogenic LRRK2 promotes NET formation during chemically induced intestinal injury without increasing neutrophil recruitment, and which LRRK2-associated downstream signaling pathway mediates this effect, remain unresolved.

Here, we used DSS-induced intestinal inflammation to determine how PD-associated LRRK2 G2019S alters neutrophil effector function in the inflamed gut. We found that LRRK2 G2019S increased colonic NET formation without increasing neutrophil infiltration and that NET-targeting interventions partially reduced intestinal pathology and enteric α-synuclein accumulation. Mechanistically, LRRK2 G2019S neutrophils exhibited a cell-intrinsic, kinase-dependent NET-hyperresponsive phenotype associated with increased RAB10 Thr73 phosphorylation, whereas phosphomimetic RAB10 was sufficient to enhance NET release. MPO–HOCl activity was required for the enhanced NET phenotype, and pathway perturbation functionally placed MPO–HOCl downstream of LRRK2–RAB10 signaling. Three-dimensional imaging further showed that LRRK2 kinase activity promotes increased co-occurrence of MPO, and pRAB10-associated MPO, with DNA^{+} regions during NET formation. Together, these findings identify a neutrophil-centered LRRK2–RAB10–MPO pathway that connects PD-associated kinase hyperactivity to peripheral intestinal inflammation and a PD-relevant enteric α-synuclein phenotype.

Results

LRRK2 G2019S aggravates recurrent DSS colitis and increases colonic NET formation without increasing neutrophil infiltration

To determine whether the PD-associated LRRK2 G2019S mutation alters host responses to recurrent intestinal injury, we subjected LRRK2 G2019S transgenic ($Tg^{LRRK2\ G2019S}$) and non-transgenic (NTg) mice to repeated DSS treatment. Although body-weight changes were broadly comparable between genotypes, LRRK2 G2019S mice developed more severe inflammatory pathology, including higher clinical scores, increased fecal lipocalin-2 and more severe histopathology, together with a trend toward greater colon shortening (Fig. 1A–D and Supplementary Fig. 1A, B). Repeated DSS treatment was also associated with increased colonic α-synuclein expression in LRRK2 G2019S mice (Supplementary Fig. 1C). Among the cytokines examined, colonic IL-6 and IL-17A were increased in LRRK2 G2019S mice, whereas other inflammatory cytokines were comparable between genotypes (Fig. 1E and Supplementary Fig. 1D). Consistent with the increased IL-17A level, the frequency of IL-17A-producing $CD4^+$ T cells was higher in the lamina propria of LRRK2 G2019S mice (Fig. 1F).

We next asked whether this exacerbated inflammatory phenotype reflected increased neutrophil recruitment or altered neutrophil effector function. Because NETs have been implicated in IBD[35], we quantified colonic NET formation by immunofluorescence. DSS-treated LRRK2 G2019S mice showed a trend toward increased colonic NET formation compared with NTg controls (Fig. 1G). This increase was not explained by greater neutrophil accumulation, because both the percentage and number of lamina propria neutrophils were similar between genotypes (Fig. 1H). Other immune cell populations examined were also comparable (Supplementary Fig. 2A, B). Thus, LRRK2 G2019S amplifies inflammatory pathology during recurrent DSS injury without a corresponding increase in neutrophil infiltration; the accompanying increase in colonic NET formation was of borderline significance in this model and is established more firmly in the acute setting below.

Enhanced NET formation precedes overt disease divergence during acute DSS colitis

To determine whether increased NET formation was secondary to more severe disease or represented an early neutrophil phenotype, we next examined an acute DSS-induced colitis. In contrast to repeated DSS exposure, acute DSS treatment induced comparable weight loss, clinical scores, fecal lipocalin-2 levels, colon shortening, and histopathology in NTg and LRRK2 G2019S mice (Fig. 2A–D). Colonic cytokine levels were also similar between genotypes (Fig. 2E). Despite this comparable overall inflammatory burden, colonic NET formation was already elevated in LRRK2 G2019S mice (Fig. 2F). As observed in the repeated DSS model, neutrophil infiltration and other lamina propria immune cell

populations were not detectably increased (Fig. 2G and Supplementary Fig. 2C). These data indicate that enhanced NET formation is an early LRRK2 G2019S-associated neutrophil phenotype that precedes overt genotype-dependent differences in acute disease severity.

NET targeting partially ameliorates colitis and reduces enteric α-synuclein accumulation in LRRK2 G2019S mice

Because NET formation can exacerbate colitis[37,38], we next tested whether NETs contribute to LRRK2 G2019S-associated intestinal pathology. DNase I was administered during DSS treatment to degrade extracellular DNA and NET structures (Fig. 3A). DNase I treatment ameliorated colitis symptoms in LRRK2 G2019S mice, as shown by improved clinical scores, longer colons, and reduced spleen weight, with a trend toward milder histopathology (Fig. 3B–D, Supplementary Fig. 3A). In contrast, DNase I had minimal effects in NTg mice. Because DNase I was administered during the DSS exposure periods, NET levels measured at the terminal collection time point were similar between DNase I- and vehicle-treated mice (Supplementary Fig. 3B), consistent with transient enzymatic degradation rather than sustained suppression of neutrophil activation. To further evaluate the contribution of NETs, LRRK2 G2019S mice deficient in peptidylarginine deiminase 4 (PAD4) were subjected to repeated DSS treatment. Although PAD4 deficiency did not significantly alter clinical scores and colon shortening, it reduced disease severity as reflected by less weight loss and milder histopathology in LRRK2 G2019S mice (Fig. 3E, Supplementary Fig. 4A–B). As expected, PAD4-deficient LRRK2 G2019S mice showed markedly reduced colonic NET formation (Supplementary Fig. 4C). Notably, both NET-targeting approaches—pharmacologic degradation with DNase I and genetic PAD4 deficiency—reduced colonic α-synuclein accumulation in LRRK2 G2019S mice (Fig. 3F–G).

Because NETs are also involved in host defense during pathogen-induced gut inflammation[39], we tested whether microbiota-derived cues are required for NET formation during DSS-induced colitis (Supplementary Fig. 5A). After repeated DSS treatment, NETs were virtually absent in germ-free mice, regardless of LRRK2 G2019S expression (Supplementary Fig. 5B). Moreover, enteric α-synuclein levels did not differ significantly between DSS-treated NTg and LRRK2 G2019S mice under germ-free conditions (Supplementary Fig. 5C). These findings indicate that microbiota-derived inflammatory signals are required for colonic NET formation and for the subsequent α-synuclein accumulation observed in LRRK2 G2019S mice during intestinal inflammation.

Collectively, these results show that NET formation contributes to LRRK2 G2019S-associated intestinal pathology and support a mechanistic link between neutrophil NETosis, intestinal inflammation, and enteric α-synuclein accumulation.

LRRK2 G2019S promotes NET formation through kinase-dependent RAB10 phosphorylation

The absence of increased neutrophil infiltration in DSS-treated LRRK2 G2019S mice suggested that LRRK2 G2019S may intrinsically enhance NET formation. To test this possibility, we stimulated isolated bone marrow neutrophils *ex vivo*. LRRK2 G2019S neutrophils released significantly more NETs than NTg neutrophils after ionomycin stimulation (Fig. 4A) and hyphal *Candida albicans* stimulation (Supplementary Fig. 6A), whereas PMA-induced NET formation was comparable between genotypes (Supplementary Fig. 6B). Because ionomycin-induced NETosis can involve mitochondrial pathways, we examined mitochondrial ROS, membrane potential, and ATP production. LRRK2 G2019S neutrophils showed no detectable differences in mitochondrial ROS after ionomycin stimulation (Fig. 4B), and mitochondrial membrane potential and ATP production were also unchanged (Supplementary Fig. 6C, D).

We next asked whether the increased kinase activity of LRRK2 G2019S is required for enhanced NETosis. Treatment with the LRRK2 kinase inhibitors LRRK2-IN-1 or MLi-2 significantly reduced NET production in LRRK2 G2019S neutrophils after ionomycin stimulation (Fig. 4C), indicating that LRRK2 kinase activity is necessary for the NET-promoting effect. To identify the stage of NETosis affected by LRRK2 G2019S, we examined histone H3 citrullination and GSDMD cleavage, two events involved in chromatin decondensation and release. Neither histone H3 citrullination nor GSDMD cleavage differed detectably between LRRK2 G2019S and NTg neutrophils (Supplementary Fig. 7A, B), suggesting that LRRK2 G2019S does not primarily act by increasing these canonical events.

LRRK2 phosphorylates several Rab GTPases, including RAB10, to regulate intracellular vesicle trafficking. We therefore evaluated RAB10 phosphorylation, a well-characterized readout of LRRK2 kinase activity[40]. RAB10 phosphorylation was significantly increased only in ionomycin-stimulated LRRK2 G2019S neutrophils (Fig. 4D), consistent with the kinase-inhibitor experiments showing that LRRK2 activity promotes NET formation. Because LRRK2–RAB10 signaling regulates immune responses in phagocytes[41], we next tested whether RAB10 phosphorylation is sufficient to enhance NETosis. HL-60 cells expressing RAB10 mutants were generated by lentiviral transduction (Supplementary Fig. 8A). After differentiation into neutrophil-like cells, cells expressing phosphomimetic RAB10 (T73E) released significantly more NETs after ionomycin stimulation than cells expressing wild-type RAB10, whereas cells expressing phospho-null RAB10 (T73A) showed no detectable increase (Fig. 4E). Together, these findings support RAB10 phosphorylation as a downstream component of the LRRK2 G2019S-associated NET-promoting pathway.

LRRK2 kinase activity promotes phosphorylated RAB10–MPO co-occurrence and MPO redistribution toward DNA$^+$ regions during NET formation

RAB10 regulates vesicular trafficking during immune cell activation[41]. We therefore asked whether phosphorylated RAB10 (pRAB10) is spatially associated with MPO-containing compartments during NET formation. Neutrophils were stimulated with ionomycin, and the three-dimensional distributions of pRAB10 and MPO were analyzed in confocal z-stacks. Following ionomycin stimulation, pRAB10 and MPO signals showed sustained spatial co-occurrence for up to 1 h. The Manders' colocalization coefficients were significantly increased in LRRK2 G2019S neutrophils compared with NTg neutrophils

(Fig. 5A–C), indicating enhanced spatial association between pRAB10 and MPO-containing compartments in LRRK2 G2019S neutrophils during NET formation.

We next examined whether this spatial association depended on LRRK2 kinase activity. Treatment with the LRRK2 kinase inhibitor MLi-2 markedly reduced pRAB10 levels (Supplementary Fig. 8B) and also substantially reduced the co-occurrence of the residual MPO signal with pRAB10 (Fig. 5D–F). Thus, LRRK2 kinase activity determines both the abundance of pRAB10 and its spatial association with MPO-containing compartments.

To define the subcellular compartments in which this association occurred, we separately quantified pRAB10–MPO co-occurrence within $CD63^+$ azurophilic granule regions and DNA^+ regions. Within $CD63^+$ regions, pRAB10–MPO co-occurrence was significantly increased in ionomycin-stimulated LRRK2 G2019S neutrophils compared with NTg neutrophils and was also reduced by MLi-2 treatment (Fig. 5D, G and H), consistent with the whole-cell analysis.

Consistent with this, MPO co-occurrence with DNA^+ regions showed a clear dependence on LRRK2 kinase activity. MPO–DNA co-occurrence increased after ionomycin stimulation in LRRK2 G2019S neutrophils, whereas this increase was less evident in NTg neutrophils. MLi-2 significantly reduced MPO–DNA co-occurrence in LRRK2 G2019S neutrophils (Fig. 5I). Similarly, pRAB10–MPO co-occurrence within DNA^+ regions was reduced by LRRK2 kinase inhibition (Fig. 5J, K). These findings indicate both the association of pRAB10 with MPO-containing granules and the increased co-occurrence of MPO, and of pRAB10-associated MPO, with DNA^+ regions require LRRK2 kinase activity. These changes were not attributable to a change in the size of the DNA^+ compartment: total DNA^+ volume per cell did not increase after ionomycin stimulation and was not altered by MLi-2 treatment (Supplementary Fig. 8C). Together, these results support a model in which enhanced LRRK2 kinase activity and RAB10 phosphorylation facilitate the redistribution of MPO-containing granule material toward DNA^+ regions during NET formation.

LRRK2 G2019S-driven NETosis requires MPO–HOCl signaling downstream of calcium mobilization

We next sought to position LRRK2-pRAB10 signaling within established NETosis pathways. Extracellular calcium is required for ionomycin-induced NETosis[42], and accordingly, spread-form NETs were not observed in neutrophils stimulated in calcium-free medium (Fig. 6A). However, in the presence of the intracellular calcium chelator BAPTA-AM, LRRK2 G2019S neutrophils still produced more NETs than NTg neutrophils (Fig. 6B). These findings suggest that although calcium influx is required to initiate ionomycin-induced NETosis, the enhanced NET-forming phenotype conferred by LRRK2 G2019S is maintained downstream of, or in parallel with, intracellular calcium mobilization.

Release of decondensed chromatin during NETosis requires pore formation by cleaved gasdermin D (GSDMD)[43,44]. Consistent with this requirement, disulfiram, an inhibitor of GSDMD pore formation[45],

significantly reduced spread-form NET release by both NTg and LRRK2 G2019S neutrophils (Fig. 6C). Thus, LRRK2 G2019S enhances NET formation within a GSDMD-dependent program rather than bypassing the canonical chromatin-release machinery.

We then examined oxidative and granule-associated mediators. ROS generated by NADPH oxidase has been implicated in ionomycin-induced NET formation[42]. Enhanced NET formation in LRRK2 G2019S neutrophils persisted in the presence of a superoxide scavenger 4-hydroxy-TEMPO (Fig. 6D). ROS and MPO can promote neutrophil elastase (NE) release from granules[46], and NE facilitates chromatin decondensation through histone degradation[47]. However, an NE inhibitor failed to eliminate the difference between LRRK2 G2019S and NTg neutrophils after ionomycin stimulation (Fig. 6E), arguing against a primary role for NE in the LRRK2 G2019S phenotype.

In contrast, MPO inhibition with 4-ABAH suppressed NET release from LRRK2 G2019S neutrophils (Fig. 6F). Consistently, scavenging hypochlorous acid (HOCl), the major oxidant product of MPO that has been reported to directly regulate NET release[48,49], abolished the difference between NTg and LRRK2 G2019S neutrophils after ionomycin stimulation (Fig. 6G). Notably, neither MPO inhibition nor HOCl scavenging substantially altered NET formation in ionomycin-stimulated NTg neutrophils. In contrast, both MPO inhibition and HOCl scavenging abolished extracellular DNA release from phosphomimetic RAB10-expressing HL-60 cells (Fig. 6H). These results identify the MPO–HOCl axis as a selective requirement for LRRK2 G2019S- and phosphomimetic RAB10-driven NET formation.

To further define the relationship between calcium signaling, HOCl, and RAB10 phosphorylation during ionomycin-stimulated NETosis, we examined RAB10 phosphorylation under pathway-specific perturbations. Ionomycin failed to induce RAB10 phosphorylation in LRRK2 G2019S neutrophils incubated in calcium-free medium (Supplementary Fig. 8D), indicating that extracellular calcium is required for activation of the LRRK2–RAB10 pathway. In contrast, HOCl scavenging did not abolish RAB10 phosphorylation (Supplementary Fig. 8E), placing HOCl downstream of, rather than upstream of, LRRK2-dependent RAB10 phosphorylation.

Together, these findings support a pathway in which calcium-dependent activation of LRRK2 and RAB10 phosphorylation promotes MPO–HOCl-dependent NET formation through a GSDMD-dependent chromatin-release program.

Discussion

Previous studies have established that the PD-associated LRRK2 G2019S variant can exacerbate intestinal inflammation and promote PD-relevant phenotypes[33,50,51]. The present study addresses a question those studies left open: which neutrophil effector program hyperactive LRRK2 engages in the inflamed gut, and through which substrate. LRRK2 G2019S enhanced NET formation without increasing neutrophil infiltration, NET-targeting interventions reduced measures of colitis severity and enteric α-synuclein accumulation, and isolated LRRK2 G2019S neutrophils displayed a cell-intrinsic, kinase-

dependent NET-hyperresponsive phenotype associated with increased RAB10 phosphorylation (Supplementary Fig. 9). Because the transgene is expressed in all cell types, the behavior of neutrophils isolated from these mice provides the primary evidence that this effect is neutrophil-intrinsic; this is consistent with, but does not substitute for, the bone-marrow transplantation experiments that established an immune-cell requirement in chronic DSS colitis[33]. These findings shift attention from inflammatory-cell recruitment toward altered neutrophil effector programming as a consequence of pathogenic LRRK2 activity in the inflamed gut.

Our findings relate to two prior studies in particular, and it is worth being precise about what each established. Mutant LRRK2 was already known to worsen chronic DSS colitis and to do so through immune cells, on the basis of bone-marrow transplantation and partial pharmacological kinase inhibition[33]; that study did not examine neutrophil effector output, NETs, or LRRK2 substrates. Separately, LRRK2 G2019S was shown to enhance neutrophil chemotaxis, NET formation and Th17-associated pathology during Citrobacter rodentium infection[34]; that study did not identify the downstream signaling that links kinase hyperactivity to NET release, and the phenotype there was accompanied by increased neutrophil recruitment. Against that background, three findings here are new. First, we identify LRRK2 kinase-dependent RAB10 Thr73 phosphorylation as a substrate-level mechanism for enhanced NET formation, with phosphomimetic RAB10 sufficient to reproduce the effect in a human neutrophil-like line. Second, we place the MPO–HOCl axis downstream of RAB10 phosphorylation as a selective requirement for the enhanced phenotype. Third, in the DSS model the increase in NET formation occurred without a detectable increase in colonic neutrophil abundance, indicating that altered effector output, rather than recruitment, can be the dominant consequence of LRRK2 hyperactivity in a non-infectious setting. NET-targeting interventions also reduced enteric α-synuclein, connecting this effector program to a PD-relevant intestinal readout.

A key issue in the LRRK2 field is why different inflammatory models produce distinct phenotypic outcomes. Increased LRRK2 kinase activity has been associated with enhanced leukocyte recruitment during microbial infection[22], whereas we observed no detectable differences in the immune-cell populations examined in DSS-treated colons. Instead, LRRK2 G2019S increased NET formation during acute DSS colitis before overt genotype-dependent differences in disease severity became apparent. This temporal separation argues against increased NETosis being simply a consequence of more severe tissue injury and raises the possibility that early NET accumulation contributes to the subsequent escalation of inflammation during recurrent challenge. The increased IL-17A levels and frequency of IL-17A-producing $CD4^+$ T cells observed after repeated DSS treatment may reflect this NET-rich inflammatory environment, because NETs and extracellular histones can promote Th17 differentiation[52,53]. Nevertheless, LRRK2 G2019S can also affect other myeloid programs that influence Th17 responses[54], and cell-specific approaches will be required to define how neutrophils interact with other immune populations in this model. This context dependence may also extend to the relationship between intestinal inflammation and central pathology. In LRRK2 G2019S BAC transgenic mice, DSS colitis has been reported to induce neuroinflammatory and nigrostriatal abnormalities without clear

exacerbation of these central phenotypes by the kinase-activating mutation[55]. Our study addresses a different compartment and disease stage: the LRRK2 G2019S-dependent phenotypes identified here involve intestinal NET formation, colitis severity, and enteric α-synuclein accumulation, whereas nigrostriatal endpoints were not examined. Host sex may add a further layer to this context dependence, because the interaction between prodromal intestinal inflammation and LRRK2 G2019S has been reported to be male-biased[51]. Together, these observations emphasize that the consequences of pathogenic LRRK2 activity may be compartment-, stimulus-, sex-, and disease-stage dependent, and that peripheral inflammatory phenotypes need not directly predict the magnitude of subsequent central nervous system pathology.

The convergence of DNase I treatment, PAD4 deficiency, and germ-free conditions supports a functional relationship among microbiota-dependent NET formation, intestinal inflammation, and enteric α-synuclein accumulation. Both DNase I treatment and PAD4 deficiency reduced α-synuclein accumulation in LRRK2 G2019S mice, whereas germ-free conditions abolished detectable colonic NET formation and loss of the genotype-dependent increase in enteric α-synuclein. Together, these converging interventions identify a cellular mechanism linking intestinal inflammation to a PD-relevant pathological feature. Consistent with this interpretation, chronic peripheral immune challenge has been shown to increase enteric α-synuclein accumulation and phosphorylation in LRRK2 G2019S mice without loss of enteric neurons[56], indicating that inflammatory input can alter enteric α-synuclein at a pre-degenerative stage in the context of a PD-associated kinase. However, our study does not establish that NET inhibition prevents later brain α-synuclein pathology or motor dysfunction. Moreover, the reduction in enteric α-synuclein after NET targeting may partly reflect an overall attenuation of inflammatory injury rather than a direct effect of NET components on α-synuclein regulation. Longitudinal studies linking intestinal NET modulation to subsequent central nervous system pathology will therefore be important for determining whether this peripheral immune pathway contributes to PD progression.

Our mechanistic findings identify RAB10 phosphorylation as a previously unrecognized component of NET regulation. LRRK2–RAB10 signaling regulates several membrane-trafficking processes, including stressed lysosomes[13] and macropinosomes [41], and phosphorylation of RAB10 can alter its interactions with downstream effector proteins[41,57,58]. In neutrophils, LRRK2 G2019S selectively increased RAB10 Thr73 phosphorylation after ionomycin stimulation, whereas LRRK2 kinase inhibition reduced both RAB10 phosphorylation and enhanced NET formation. In parallel, phosphomimetic RAB10 was sufficient to increase NET release in differentiated HL-60 cells, whereas phospho-null RAB10 did not produce a comparable increase. These findings provide a mechanistic bridge between a canonical LRRK2 kinase substrate and neutrophil effector function.

The MPO–HOCl axis emerged as an additional selective requirement for LRRK2 G2019S-enhanced NET formation. This finding is particularly relevant in light of recent structural and functional work showing that MPO can act directly on chromatin by binding nucleosomes and promoting the chromatin decondensation required for NET formation[59]. Our imaging data are consistent with such a mechanism:

the fraction of MPO signal co-occurring with DNA⁺ regions increased after stimulation in LRRK2 G2019S neutrophils and was reduced by LRRK2 kinase inhibition, as was the association between residual pRAB10 and MPO-containing compartments. Because the DNA⁺ compartment did not expand under these conditions, this change is unlikely to reflect altered segmentation of the DNA⁺ region and is better explained by redistribution of MPO toward DNA⁺ regions. One interpretation is that LRRK2-dependent RAB10 phosphorylation influences the trafficking or deployment of MPO-containing azurophilic granule material, thereby facilitating MPO access to chromatin, where MPO may contribute through both HOCl generation and direct chromatin remodeling. This model accounts for the preferential suppression of the enhanced NET phenotype by MPO inhibition and HOCl scavenging, whereas NE inhibition did not eliminate the genotype-dependent difference. Two observations further support functional ordering of the pathway. First, HOCl scavenging did not detectably reduce RAB10 phosphorylation, arguing against HOCl acting upstream of LRRK2–RAB10 signaling. Second, MPO inhibition or HOCl scavenging suppressed the NET-promoting effect of phosphomimetic RAB10. Together, these findings functionally place MPO–HOCl activity downstream of, or as an essential effector of, RAB10 phosphorylation during enhanced NET formation. Whether pRAB10 directly controls MPO-containing granule trafficking or regulates the direct chromatin-remodeling activity of MPO remains to be established.

Placing these findings within the gut–brain axis highlights the potential neurobiological relevance of a peripheral neutrophil phenotype. Enteric α-synuclein accumulation has been proposed as an early feature of body-first PD, in which pathological processes may arise in the gastrointestinal tract before involvement of the central nervous system[1–3]. Our findings suggest that a PD-associated LRRK2 variant can influence this enteric phenotype indirectly by altering innate immune-cell effector function rather than solely through neuron-autonomous mechanisms. NETs provide a plausible interface because they expose the intestinal mucosa to extracellular chromatin, histones, MPO-derived oxidants, and inflammatory signals capable of amplifying tissue injury and Th17-associated responses[52,53]. Importantly, our data do not establish propagation of pathology from the intestine to the brain. Rather, they identify a peripheral immune mechanism that can modify the inflammatory environment in which PD-relevant enteric α-synuclein changes arise.

From a translational perspective, the sensitivity of the enhanced NET phenotype to LRRK2 kinase inhibition raises the possibility that therapeutic LRRK2 inhibition could modulate neutrophil effector function in peripheral tissues in addition to its effects on other LRRK2-expressing cell populations. Because RAB10 phosphorylation can be measured in human peripheral immune cells as a pharmacodynamic marker of LRRK2 activity[40], defining how this signaling axis influences neutrophil function in carriers of pathogenic LRRK2 variants may provide a useful bridge between LRRK2 target engagement and peripheral immune responses relevant to PD. This bridge, however, may depend on the conditions under which phosphorylation is measured: in fresh peripheral blood neutrophils from 101 participants, basal RAB10 Thr73 phosphorylation was increased more than fourfold in carriers of the LRRK2 R1441G mutation but was not significantly elevated in 21 G2019S carriers, leading the authors to conclude that additional readouts or assays may be needed to detect the more modest kinase activation

conferred by G2019S[60]. Our findings suggest one such direction, because the genotype-dependent increase in RAB10 phosphorylation we observed emerged only after neutrophil stimulation rather than under resting conditions, raising the possibility that stimulation-dependent pRAB10 measurement, or a downstream functional readout such as NET release, offers greater sensitivity for G2019S than basal phosphorylation alone.

Overall, this study identifies a neutrophil-centered pathway through which PD-associated LRRK2 G2019S enhances intestinal inflammation. LRRK2 G2019S confers a cell-intrinsic, kinase-dependent NET-hyperresponsive phenotype associated with increased RAB10 Thr73 phosphorylation, while MPO–HOCl activity is required for the enhanced NET response. *In vivo*, increased NET formation occurs without greater neutrophil recruitment, precedes overt genotype-dependent disease divergence, and is functionally associated with colitis severity and enteric α-synuclein accumulation.

These findings connect pathogenic LRRK2 kinase activity to peripheral neutrophil effector programming and identify the LRRK2–RAB10–MPO axis as a candidate mechanism at the interface between intestinal inflammation and PD-relevant enteric pathology. Because LRRK2 kinase activity, MPO, and NETs themselves are each addressable with agents already in clinical use or clinical development, this peripheral axis offers a potential point of intervention that does not require access to the central nervous system. Determining whether modulation of this pathway alters subsequent central α-synuclein pathology or neurological dysfunction will require longitudinal gut-to-brain studies.

Methods

Animals

FVB/NJ and FVB/N-Tg(LRRK2*G2019S)1Cjli/J were housed under specific-pathogen-free conditions with a 12 h light–dark cycle at the Animal Resource Center at National Taiwan University and the National Center for Biomodels, NIAR, Taiwan. FVB/N-Tg(LRRK2*G2019S)1Cjli/J were crossed with C57BL/6 mice to generate mice carrying transgenic LRRK2 G2019S on a B6 background. These mice were then crossed with *Padi4*$^{-/-}$ mice (B6.Cg-Padi4tm1.1Kmow/J) to generate mice carrying LRRK2 G2019S and PAD4 deficiency. All experiments were performed in accordance with protocols approved by the Institutional Animal Care and Use Committee (IACUC) of National Taiwan University (approval numbers NTU-112–017 and # NTU-112–049). All procedures complied with the relevant institutional and national guidelines and regulations for the care and use of laboratory animals. This study did not involve human participants, human data, or human tissue. Reporting of the animal experiments follows the ARRIVE Essential 10 guidelines.

Colitis models and in vivo NET targeting

To induce colitis, mice were given DSS (36,000–50,000 Da; MP Biomedicals) in drinking water at the indicated concentration (0.5%, 1.5%, or 3%, w/v) for 7 days, followed by normal drinking water to

complete one DSS cycle. For repeated DSS treatment, mice received three DSS cycles, each separated by 7 days of normal drinking water. Clinical scores were determined based on stool consistency and rectal bleeding[61]. For NET degradation, mice were intravenously injected with 250 U DNase I every 2 days during the DSS treatment periods. Vehicle-control mice received PBS. Unless otherwise indicated, DSS administration was initiated when mice were 8 weeks old. Only male FVB-background mice were used in all experiments, whereas both male and female C57BL/6-background mice were included. For germ-free experiments, 12-month-old female mice were subjected to DSS treatment.

Histology and histopathological scoring

Distal colons were fixed in 10% formaldehyde overnight at room temperature and embedded in paraffin. Tissue sections were stained with hematoxylin and eosin. Histopathology was scored as previously described[61] based on inflammation, inflammatory extent, and crypt damage.

Cytokine and lipocalin-2 measurements

Distal colon tissue was homogenized in RIPA lysis buffer and centrifuged at 16,000 × g for 10 min at 4°C. Supernatants were collected, and protein concentrations were determined using a BCA assay (cat# 23225, Thermo Scientific). Samples were stored at − 80°C until analysis. Cytokine levels were measured using multiplex immunoassays or ELISA kits (cat# 430801, 430901, 431301, 431411, and 432501; BioLegend).

For fecal lipocalin-2 measurements, stools were collected during the experimental period and stored at − 30°C until analysis. Stools were homogenized in 0.1% Tween-20/PBS at a ratio of 100 mg/ml and centrifuged at 9,300 × g for 20 min at 4°C. Supernatants were collected for ELISA (cat# DY1857, R&D Systems).

Isolation of intestinal and lymph node immune cells

Whole colons were collected, cut into 1-cm pieces, and washed with PBS for 2 min. All washes and treatments were performed at 37°C with shaking unless otherwise indicated. After three washes, tissues were treated with 1 mM DTT in PBS for 10 min and washed once with PBS. Tissues were transferred to 30 mM EDTA in PBS and washed for 8 min. After three EDTA/PBS washes, tissues were washed three additional times with Ca^{2+}/Mg^{2+}-containing PBS for 2 min at room temperature. To digest collagen, tissues were cut into smaller pieces and treated with 5% FBS/DMEM containing Liberase TL (38.5 µg/ml; cat# 05401020001, Roche) and DNase I (20 µg/ml; cat# DRB001, BioShop). Digestion was performed at 37°C for 45 min, and supernatants were passed through a 100-µm strainer. Tissues were further digested in digestion medium at room temperature for another 45 min, and cells were collected by centrifugation at 478 × g for 5 min. For mesenteric lymph node (MLN) cell isolation, MLNs were disrupted in digestion medium and incubated at room temperature for 45 min. The medium was passed through a 100-µm strainer to remove tissue debris, and cells were collected by centrifugation at 478 × g for 5 min.

Cell lines, lentiviral transduction, and primary neutrophil isolation

HL-60 cells were cultured in RPMI 1640 medium supplemented with 10% FBS and penicillin/streptomycin at 37°C and 5% CO_2. To differentiate HL-60 cells into neutrophil-like cells, cells were incubated in medium containing 1.3% DMSO for 5 days.

HL-60 cells were transduced by spinoculation with BaEV-pseudotyped lentivirus encoding wild-type or mutant (T73E or T73A) RAB10 constructs (SFFV-turboGFP-T2A-RAB10). TurboGFP$^+$ cells were identified as transduced cells and sorted accordingly.

Bone marrow cells were collected from mouse femurs and tibias. Bone marrow neutrophils were isolated using Histopaque 1077 and 1119 gradient solutions (cat# 10771 and 11191, Sigma).

NET formation assays

Cells were resuspended in RPMI 1640 medium and incubated in plates or on coverslips for 30 min before stimulation. For HL-60 cells, coverslips were coated with poly-L-lysine to facilitate adhesion. To induce NETosis, neutrophils were stimulated with ionomycin (cat# I0634, Sigma) or PMA (cat# P8139, Sigma) at 37°C for 3 or 4 h, respectively. For hyphal *Candida albicans* stimulation, *C. albicans* SC5314 was first incubated at 37°C for 4 h to induce hypha formation before being added to neutrophils. Where indicated, cells were pretreated for 30 min during the adhesion period with LRRK2-IN-1 (cat# 438193, Millipore), MLi-2 (cat# 5756, Tocris), disulfiram (cat# HY-B0240, MedChemExpress), neutrophil elastase inhibitor (NE inhibitor; cat# sc-215426A, Santa Cruz), 4-aminobenzoic acid hydrazide (4-ABAH; cat# 14845, Cayman Chemical), or dihydrolipoic acid (DHLA; cat# sc-207581, Santa Cruz) before stimulation. BAPTA-AM (cat# 2787, Tocris) or 4-hydroxy-TEMPO (cat# 176141, Sigma) was added during stimulation where indicated.

Immunofluorescence staining and image analysis

For detection of NETs in DSS-treated colons, distal colon samples were embedded in frozen section compound (cat# 95057-838, VWR International) and stored at − 30°C until sectioning. Frozen sections were cut at 8 µm, mounted on silane-coated slides, and fixed with 4% PFA. Sections were permeabilized with 0.1% Triton X-100 in PBS, washed, and blocked with PBS containing 10% donkey serum for 1 h at room temperature. Primary antibodies against MPO (cat# AF3667, R&D Systems) and citrullinated histone H3 (citH3; cat# ab5103, Abcam) were diluted 1:200 in blocking buffer and incubated overnight at 4°C. After three washes, sections were incubated with secondary antibodies diluted 1:500 for 1 h at room temperature. Sections were then washed three times and stained with Hoechst 33342 (1:2000; H3570, Invitrogen) for 5 min. Slides were mounted with mounting medium (cat# S3023, Dako) and coverslipped. Immunofluorescence signal areas were quantified using ImageJ by thresholding. NETs were defined as areas with colocalized DNA, MPO, and citH3 signals and are shown in yellow in the figures.

For *in vitro* NET formation assays, the same staining procedure was used with modified antibody dilutions. Primary antibodies against MPO were diluted 1:80, and antibodies against citH3 and DNA/histone H1 (cat# MAB3684, Sigma) were diluted 1:400. Secondary antibodies were diluted 1:1000, and Hoechst 33342 was diluted 1:10,000. Spread-form NETs were identified based on neutrophil morphology and colocalized DNA, MPO, and citH3 signals. For colocalization analysis, primary antibodies against MPO and phospho-RAB10 (T73) (cat# ab230261, Abcam) were diluted 1:500, and antibodies against CD63 (cat# sc-5275, Santa Cruz) were diluted 1:50. Images were taken with Leica TCS SP8. Imaris was used to analyze colocalization between immunofluorescence signals by thresholding. Manders coefficient A-B stands for the fraction of A intensity colocalized with B signals. DNA^+ and MPO^+ regions were defined by thresholding the Hoechst 33342 and MPO channels, respectively, and the total segmented volume of each channel was quantified per cell in the same z-stacks used for colocalization analysis.

Secondary antibodies used for staining included Alexa Fluor 488 donkey anti-goat IgG (H + L) (cat# A-11055, Invitrogen), Alexa Fluor 488 donkey anti-rabbit IgG (H + L) (cat# A-21206, Invitrogen), Alexa Fluor 568 donkey anti-rabbit IgG (H + L) (cat# A-10042, Invitrogen), Alexa Fluor 568 donkey anti-mouse IgG (H + L) (cat# A-10037, Invitrogen), Alexa Fluor 647 donkey anti-goat IgG (H + L) (cat# A-21447, Invitrogen), and Alexa Fluor 647 donkey anti-rabbit IgG (H + L) (cat# ab150075, Abcam).

Extracellular DNA release assay

HL-60 cells were incubated with or without 4-ABAH and DHLA at 37°C for 30 min before ionomycin stimulation in 96-well plates for 3 h. 10% Triton X-100 medium was used to treat cells as the positive control. 20 Kunitz DNase I was added after 2 h. 0.5 μM SYTOX deep red (cat# S11381, Invitrogen) was used to stain extracellular DNA for 15 min before the end of stimulation. All groups were performed in duplicate wells. Fluorescence was detected by SpectraMax i3x with Ex/Em wavelengths at 660/682 nm. Extracellular DNA level was quantified as: [(intensity of cells + stimuli) − (intensity of cells + stimuli + DNase I)] / (intensity of cells + Triton X-100)

ATP measurement

Cells were stimulated with or without ionomycin for 30 min at 37°C and then lysed with ddH_2O. ATP concentrations were measured using an ATP determination kit (cat# A22066, Invitrogen), followed by luminescence analysis on a SpectraMax i3x instrument.

Flow cytometry

Immune cells isolated from DSS-treated tissues were resuspended in FACS buffer (1% BSA and 0.1% NaN_3 in PBS) and incubated with rat anti-mouse CD16/CD32 antibody (1:100; cat# 553142, BD Biosciences) on ice to block Fc receptors. Cells were then stained with fluorescence-conjugated antibodies.

For intracellular cytokine staining, isolated cells were stimulated with 50 nM PMA and 1 μg/ml ionomycin in the presence of 1× brefeldin A (cat# 420601, BioLegend) for 5 h at 37°C. After stimulation, cells were

collected and stained with antibodies against surface markers. Fixation and permeabilization were performed using the Cytofix/Cytoperm Fixation/Permeabilization Kit (cat# 554714, BD Biosciences) according to the manufacturer's protocol before intracellular staining overnight at 4°C.

The following primary antibodies were used: CD45 (cat# 103115, 103106, and 103113, BioLegend), CD3 (cat# 100236, BioLegend), CD11b (cat# 101212, BioLegend), CD4 (cat# 100414, BioLegend), CX3CR1 (cat# 149019, BioLegend), I-A/I-E (cat# 107605, BioLegend), TCRγ/δ (cat# 118105, BioLegend), CD8α (cat# 100707, BioLegend), CD11c (cat# 117318, BioLegend), Ly6G (cat# 127618, BioLegend), IL-17A (cat# 506903, BioLegend), and IgG1 kappa isotype control antibody (cat# 12-4301-81, Invitrogen).

For mitochondrial analysis, 500 nM MitoSOX Red (cat# M36008, Invitrogen) was added during stimulation and incubated with cells for 30 min. TMRE (cat# T669, Invitrogen) was added at a final concentration of 25 nM for 20 min after stimulation. Cells were pelleted and washed before analysis.

All data were acquired on a BD FACSCanto II and analyzed using FlowJo.

Immunoblotting

The distal 1 cm of the colon was homogenized in RIPA buffer supplemented with protease and phosphatase inhibitors. Cells were lysed in RIPA buffer and incubated for 15 min with agitation at 4°C. Supernatants were collected after centrifugation at 16,000 × g for 10 min at 4°C. Protein concentrations were determined using the BCA assay. Protein samples (20 µg or 5–10 µg) were mixed with loading buffer and incubated at 100°C for 10 min before immunoblotting. Samples were separated on 10–15% SDS-PAGE gels and transferred to PVDF membranes. Membranes were blocked with 5% milk or 5% BSA (for phosphorylated proteins) in TBST, followed by incubation with primary antibodies overnight at 4°C and secondary antibodies for 1 h at room temperature. Images were acquired using a UVP ChemStudio PLUS system (Analytik Jena) and analyzed with VisionWorks. To compare values across independent experiments, each band was normalized to the selected control, usually the average of NTg-DSS samples in *in vivo* experiments or NTg-stimulated samples in *ex vivo* experiments. The following antibodies were used: α-synuclein (cat# 2642, Cell Signaling Technology), RAB10 (cat# ab237703, Abcam), phospho-RAB10 (T73) (cat# ab230261, Abcam), β-actin (cat# GTX109639, GeneTex), gasdermin D (cat# ab209845, Abcam), gasdermin D (cat# A18281, Abclonal), citrullinated histone H3 (R2 + R8+R17) (cat# ab5103, Abcam), histone H3 (cat# ab1791, Abcam), and goat anti-rabbit IgG (1:5000; cat# 111-035-003, Jackson ImmunoResearch).

Statistical analysis

All statistical analyses were performed in GraphPad Prism. Comparisons between two groups used unpaired two-tailed Student's t tests, and comparisons among three or more groups used one-way or two-way analysis of variance followed by Tukey's multiple-comparisons test. The significance threshold was $\alpha = 0.05$, and data are presented as mean ± s.e.m. For in vivo experiments, n denotes the number of mice; for ex vivo and cell-culture experiments, n denotes the number of independent experiments, as stated in each figure legend.

Declarations

Data Availability

All data generated or analyzed during this study are included in this article and its supplementary material. The raw datasets generated and analyzed during the current study are available from the corresponding author on reasonable request. Plasmids and cell lines generated in this study are available from the corresponding author on reasonable request.

Acknowledgements

We thank the National Center for Biomodels, NIAR, Taiwan, for technical support with germ-free mouse experiments. We also thank the Animal Resource Center, NTU; Technology Commons, College of Life Science, NTU; Instrumentation Center, NTU; and the Academia Sinica Inflammation Core Facility, IBMS, for their technical assistance. This work was supported by grants from the National Science and Technology Council (NSTC), Taiwan (114-2320-B-002-060-MY3, 114-2314-B-002-046, 114-2811-B-002-194, 115-2314-B-002-018, and 115-2811-B-002-150 to H.-S.C.). The funding body had no role in the design of the study; in the collection, analysis, or interpretation of data; or in writing the manuscript.

Author contributions

Y.-K.C. and H.-S.C. conceived and designed the study. Y.-K.C. performed most experiments and analyzed the data. K.-Q.L., P.-J.L., M.-J.C., C.-Y.L., Y.-W.H., J.-M.W., S.-L.M., Y.-H.L., and J.-P.S. contributed to experiments and data analysis. H.-Y.C. contributed to multiplex immunoassays. H.-A.S., C.-W.C., and S.L. generated RAB10-mutant HL-60 cells and provided technical expertise. C.-H.L. provided germ-free mice and contributed to study design. Y.-K.C. and H.-S.C. wrote the manuscript with input from all authors. H.-S.C. supervised the study. All authors read and approved the final manuscript.

Competing interests

The authors have declared that no competing interests exist.

References

1. Braak, H., Rub, U., Gai, W. P. & Del Tredici, K. Idiopathic Parkinson's disease: possible routes by which vulnerable neuronal types may be subject to neuroinvasion by an unknown pathogen. *J Neural Transm (Vienna)* **110**, 517–536 (2003).
2. Borghammer, P. The brain-first vs. body-first model of Parkinson's disease with comparison to alternative models. *J Neural Transm (Vienna)* **130**, 737–753 (2023).
3. Svensson, E. *et al.* Vagotomy and subsequent risk of Parkinson's disease. *Ann Neurol* **78**, 522–529 (2015).

4. Yan, F. *et al.* Gastrointestinal nervous system α-synuclein as a potential biomarker of Parkinson disease. *Medicine (Baltimore)* **97**, e11337 (2018).
5. Braak, H., de Vos, R. A. I., Bohl, J. & Del Tredici, K. Gastric α-synuclein immunoreactive inclusions in Meissner's and Auerbach's plexuses in cases staged for Parkinson's disease-related brain pathology. *Neurosci Lett* **396**, 67–72 (2006).
6. Devos, D. *et al.* Colonic inflammation in Parkinson's disease. *Neurobiol Dis* **50**, 42–48 (2013).
7. Chiang, H. L. & Lin, C. H. Altered Gut Microbiome and Intestinal Pathology in Parkinson's Disease. *J Mov Disord* **12**, 67–83 (2019).
8. Kim, S. *et al.* Transneuronal Propagation of Pathologic alpha-Synuclein from the Gut to the Brain Models Parkinson's Disease. *Neuron* **103**, 627-641 e627 (2019).
9. Matheoud, D. *et al.* Intestinal infection triggers Parkinson's disease-like symptoms in Pink1(-/-) mice. *Nature* **571**, 565–569 (2019).
10. Lin, J. C., Lin, C. S., Hsu, C. W., Lin, C. L. & Kao, C. H. Association Between Parkinson's Disease and Inflammatory Bowel Disease: a Nationwide Taiwanese Retrospective Cohort Study. *Inflamm Bowel Dis* **22**, 1049–1055 (2016).
11. Peter, I. *et al.* Anti-Tumor Necrosis Factor Therapy and Incidence of Parkinson Disease Among Patients With Inflammatory Bowel Disease. *JAMA Neurol* **75**, 939–946 (2018).
12. Kluss, J. H., Mamais, A. & Cookson, M. R. LRRK2 links genetic and sporadic Parkinson's disease. *Biochem Soc Trans* **47**, 651–661 (2019).
13. Eguchi, T. *et al.* LRRK2 and its substrate Rab GTPases are sequentially targeted onto stressed lysosomes and maintain their homeostasis. *Proc Natl Acad Sci U S A* **115**, E9115–E9124 (2018).
14. Tong, Y. *et al.* Loss of leucine-rich repeat kinase 2 causes impairment of protein degradation pathways, accumulation of α-synuclein, and apoptotic cell death in aged mice. *Proc Natl Acad Sci U S A* **107**, 9879–9884 (2010).
15. Schapansky, J., Nardozzi, J. D., Felizia, F. & LaVoie, M. J. Membrane recruitment of endogenous LRRK2 precedes its potent regulation of autophagy. *Hum Mol Genet* **23**, 4201–4214 (2014).
16. Singh, F. *et al.* Pharmacological rescue of impaired mitophagy in Parkinson's disease-related LRRK2 G2019S knock-in mice. *Elife* **10**, e67604 (2021).
17. MacLeod, D. *et al.* The Familial Parkinsonism Gene LRRK2 Regulates Neurite Process Morphology. *Neuron* **52**, 587–593 (2006).
18. Matikainen-Ankney, B. A. *et al.* Altered Development of Synapse Structure and Function in Striatum Caused by Parkinson's Disease-Linked LRRK2–G2019S Mutation. *J Neurosci* **36**, 7128 (2016).
19. Smith Wanli, W. *et al.* Leucine-rich repeat kinase 2 (LRRK2) interacts with parkin, and mutant LRRK2 induces neuronal degeneration. *Proc Natl Acad Sci U S A* **102**, 18676–18681 (2005).
20. Ramonet, D. *et al.* Dopaminergic Neuronal Loss, Reduced Neurite Complexity and Autophagic Abnormalities in Transgenic Mice Expressing G2019S Mutant LRRK2. *PLoS One* **6**, e18568 (2011).

21. Novello, S. *et al.* G2019S LRRK2 mutation facilitates α-synuclein neuropathology in aged mice. *Neurobiol Dis* **120**, 21–33 (2018).
22. Shutinoski, B. *et al.* Lrrk2 alleles modulate inflammation during microbial infection of mice in a sex-dependent manner. *Sci Transl Med* **11**, eaas9292 (2019).
23. Wang, D. *et al.* Association of the LRRK2 genetic polymorphisms with leprosy in Han Chinese from Southwest China. *Genes Immun* **16**, 112–119 (2015).
24. Fava, V. M. *et al.* A Missense LRRK2 Variant Is a Risk Factor for Excessive Inflammatory Responses in Leprosy. *PLoS Negl Trop Dis* **10**, e0004412 (2016).
25. Gardet, A. *et al.* LRRK2 Is Involved in the IFN-γ Response and Host Response to Pathogens. *J Immunol* **185**, 5577 (2010).
26. Liu, W. *et al.* LRRK2 promotes the activation of NLRC4 inflammasome during Salmonella Typhimurium infection. *J Exp Med* **214**, 3051–3066 (2017).
27. Takagawa, T. *et al.* An increase in LRRK2 suppresses autophagy and enhances Dectin-1–induced immunity in a mouse model of colitis. *Sci Transl Med* **10**, eaan8162 (2018).
28. Weindel, C. G. *et al.* LRRK2 maintains mitochondrial homeostasis and regulates innate immune responses to Mycobacterium tuberculosis. *Elife* **9**, e51071 (2020).
29. Weindel, C. G. *et al.* Mitochondrial ROS promotes susceptibility to infection via gasdermin D-mediated necroptosis. *Cell* **185**, 3214-3231.e3223 (2022).
30. Nalls, M. A. *et al.* Genetic comorbidities in Parkinson's disease. *Hum Mol Genet* **23**, 831–841 (2014).
31. Hui, K. Y. *et al.* Functional variants in the LRRK2 gene confer shared effects on risk for Crohn's disease and Parkinson's disease. *Sci Transl Med* **10**, eaai7795 (2018).
32. Liu, Z. *et al.* The kinase LRRK2 is a regulator of the transcription factor NFAT that modulates the severity of inflammatory bowel disease. *Nat Immunol* **12**, 1063–1070 (2011).
33. Cabezudo, D., Tsafaras, G., Van Acker, E., Van den Haute, C. & Baekelandt, V. Mutant LRRK2 exacerbates immune response and neurodegeneration in a chronic model of experimental colitis. *Acta Neuropathol* **146**, 245–261 (2023).
34. Pei, J. *et al.* Lrrk2 G2019S mutation incites increased cell-intrinsic neutrophil effector functions and intestinal inflammation in a model of infectious colitis. *NPJ Parkinsons Dis* **11**, 267 (2025).
35. Drury, B., Hardisty, G., Gray, R. D. & Ho, G. t. Neutrophil Extracellular Traps in Inflammatory Bowel Disease: Pathogenic Mechanisms and Clinical Translation. *Cell Mol Gastroenterol Hepatol* **12**, 321–333 (2021).
36. Shafqat, A. *et al.* Neutrophil extracellular traps in central nervous system pathologies: a mini review. *Front Med (Lausanne)* **10**, 1083242 (2023).
37. Lin, E. Y. *et al.* Neutrophil Extracellular Traps Impair Intestinal Barrier Function during Experimental Colitis. *Biomedicines* **8**, 275 (2020).
38. Lai, H. J. *et al.* Histones of Neutrophil Extracellular Traps Directly Disrupt the Permeability and Integrity of the Intestinal Epithelial Barrier. *Inflamm Bowel Dis* **29**, 783–797 (2023).

39. Saha, P. *et al.* PAD4-dependent NETs generation are indispensable for intestinal clearance of Citrobacter rodentium. *Mucosal Immunol* **12**, 761–771 (2019).
40. Fan, Y. *et al.* Interrogating Parkinson's disease LRRK2 kinase pathway activity by assessing Rab10 phosphorylation in human neutrophils. *Biochem J* **475**, 23–44 (2018).
41. Liu, Z., Xu, E., Zhao, H. T., Cole, T. & West, A. B. LRRK2 and Rab10 coordinate macropinocytosis to mediate immunological responses in phagocytes. *EMBO J* **39**, e104862 (2020).
42. Gupta, A. K., Giaglis, S., Hasler, P. & Hahn, S. Efficient Neutrophil Extracellular Trap Induction Requires Mobilization of Both Intracellular and Extracellular Calcium Pools and Is Modulated by Cyclosporine A. *PLoS One* **9**, e97088 (2014).
43. Sollberger, G. *et al.* Gasdermin D plays a vital role in the generation of neutrophil extracellular traps. *Sci Immunol* **3**, eaar6689 (2018).
44. Chen, K. W. *et al.* Noncanonical inflammasome signaling elicits gasdermin D–dependent neutrophil extracellular traps. *Sci Immunol* **3**, eaar6676 (2018).
45. Hu, J. J. *et al.* FDA-approved disulfiram inhibits pyroptosis by blocking gasdermin D pore formation. *Nat Immunol* **21**, 736–745 (2020).
46. Metzler Kathleen, D., Goosmann, C., Lubojemska, A., Zychlinsky, A. & Papayannopoulos, V. A Myeloperoxidase-Containing Complex Regulates Neutrophil Elastase Release and Actin Dynamics during NETosis. *Cell Rep* **8**, 883–896 (2014).
47. Papayannopoulos, V., Metzler, K. D., Hakkim, A. & Zychlinsky, A. Neutrophil elastase and myeloperoxidase regulate the formation of neutrophil extracellular traps. *J Cell Biol* **191**, 677–691 (2010).
48. Palmer, L. J. *et al.* Hypochlorous acid regulates neutrophil extracellular trap release in humans. *Clin Exp Immunol* **167**, 261–268 (2012).
49. Akong-Moore, K., Chow, O. A., von Kockritz-Blickwede, M. & Nizet, V. Influences of chloride and hypochlorite on neutrophil extracellular trap formation. *PLoS One* **7**, e42984 (2012).
50. Lin, C. H. *et al.* Mild Chronic Colitis Triggers Parkinsonism in LRRK2 Mutant Mice Through Activating TNF-alpha Pathway. *Mov Disord* **37**, 745–757 (2022).
51. Fang, P. *et al.* Sex-dependent interactions between prodromal intestinal inflammation and LRRK2 G2019S in mice promote endophenotypes of Parkinson's disease. *Commun Biol* **7**, 570 (2024).
52. Kim, T. S. *et al.* Neutrophil extracellular traps and extracellular histones potentiate IL-17 inflammation in periodontitis. *J Exp Med* **220**, e20221751 (2023).
53. Wilson, A. S. *et al.* Neutrophil extracellular traps and their histones promote Th17 cell differentiation directly via TLR2. *Nat Commun* **13**, 528 (2022).
54. Park, J. *et al.* Parkinson disease–associated LRRK2 G2019S transgene disrupts marrow myelopoiesis and peripheral Th17 response. *J Leukoc Biol* **102**, 1093–1102 (2017).
55. Merchak, A. R. *et al.* Intestinal inflammation promotes neuroinflammation and PD-associated nigrostriatal pathology independently of LRRK2 G2019S kinase activity. *Front Cell Neurosci* **20**,

1794784 (2026).

56. Giachino, C. *et al.* Peripheral Immune Challenge Drives Enteric alpha-Synuclein and Tau Pathology in LRRK2 G2019S Mice. *Aging Dis* https://doi.org/10.14336/AD.2026.0342 (2026) doi:10.14336/AD.2026.0342.
57. Steger, M. *et al.* Systematic proteomic analysis of LRRK2-mediated Rab GTPase phosphorylation establishes a connection to ciliogenesis. *Elife* **6**, e31012 (2017).
58. Liu, Z. *et al.* LRRK2 phosphorylates membrane-bound Rabs and is activated by GTP-bound Rab7L1 to promote recruitment to the trans-Golgi network. *Hum Mol Genet* **27**, 385–395 (2018).
59. Burn, G. L. *et al.* Myeloperoxidase transforms chromatin into neutrophil extracellular traps. *Nature* **647**, 747–756 (2025).
60. Fan, Y. *et al.* R1441G but not G2019S mutation enhances LRRK2 mediated Rab10 phosphorylation in human peripheral blood neutrophils. *Acta Neuropathol* **142**, 475–494 (2021).
61. Dieleman, L. A. *et al.* Chronic experimental colitis induced by dextran sulphate sodium (DSS) is characterized by Th1 and Th2 cytokines. *Clin Exp Immunol* **114**, 385–391 (1998).

Figures

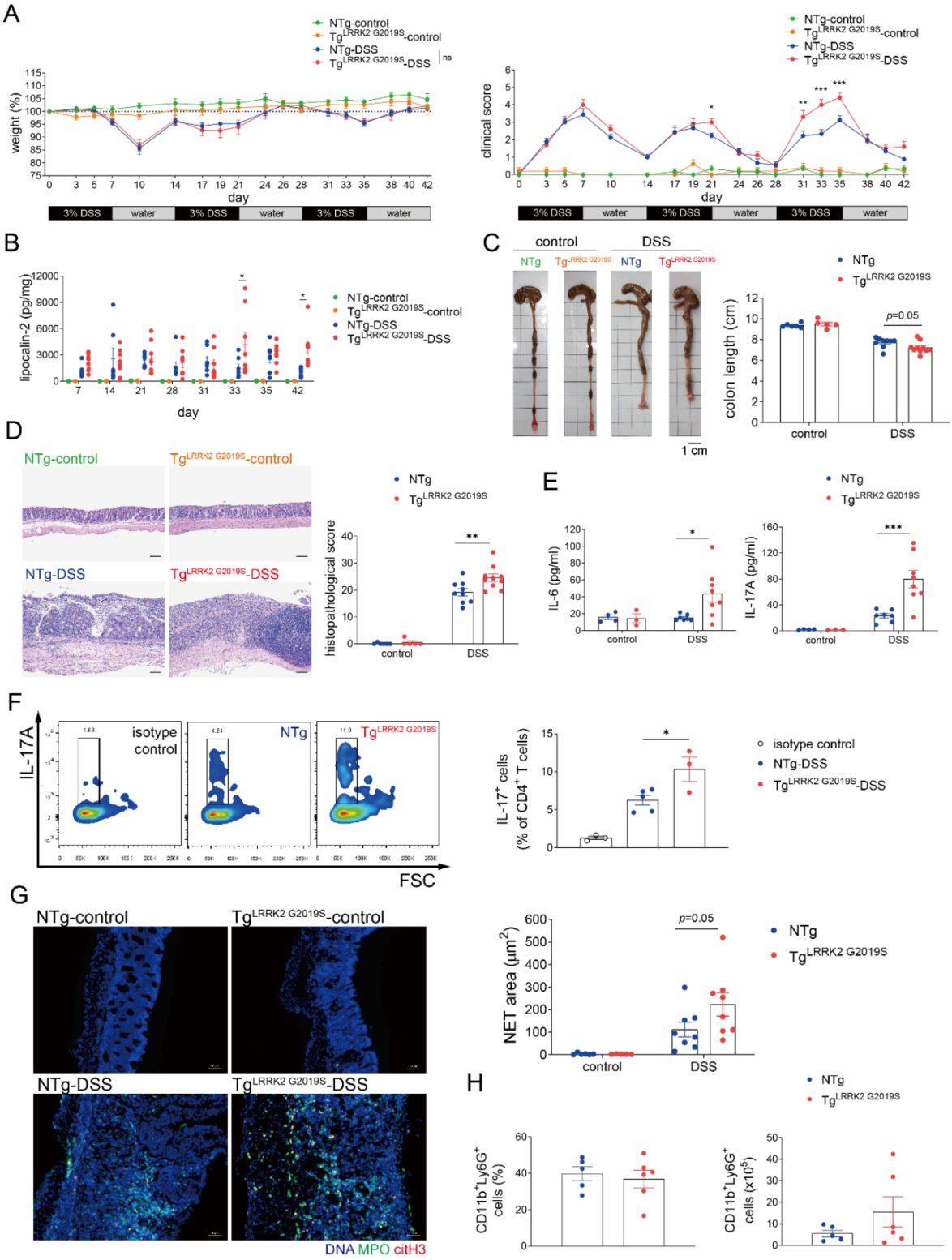


Figure 1

LRRK2 G2019S aggravates recurrent DSS-induced intestinal inflammation and increases colonic NET formation

A–E Weight change and clinical scores (**A**) and fecal lipocalin-2 levels (**B**) during repeated DSS treatment. Representative colon images and colon length quantification (**C**), representative H&E images

of distal colon and histopathology quantification (**D**), and colonic IL-6 and IL-17A levels (**E**) at the end of the experiment. **F** Percentage of IL-17A-producing $CD4^+$ T cells in the colonic lamina propria of repeated DSS-treated mice. **G** Representative immunofluorescence images and quantification of colonic NETs in mice treated with or without DSS. **H** Percentage and number of neutrophils ($CD45^+CD11b^+Ly6G^+$) in the colonic lamina propria of repeated DSS-treated mice. Data are presented as mean ± SEM. Scale bars, 100 μm in panel **D** and 50 μm in panel **G**. N = 3–6 for control groups and N = 8–10 for DSS groups in panels **A–E** and **G**; N = 3–6 for each group in panels **F** and **H**. **P* < 0.05; ***P* < 0.01; ****P* < 0.001. In panel **A**, * indicates a significant difference between DSS-treated LRRK2 G2019S and NTg mice.

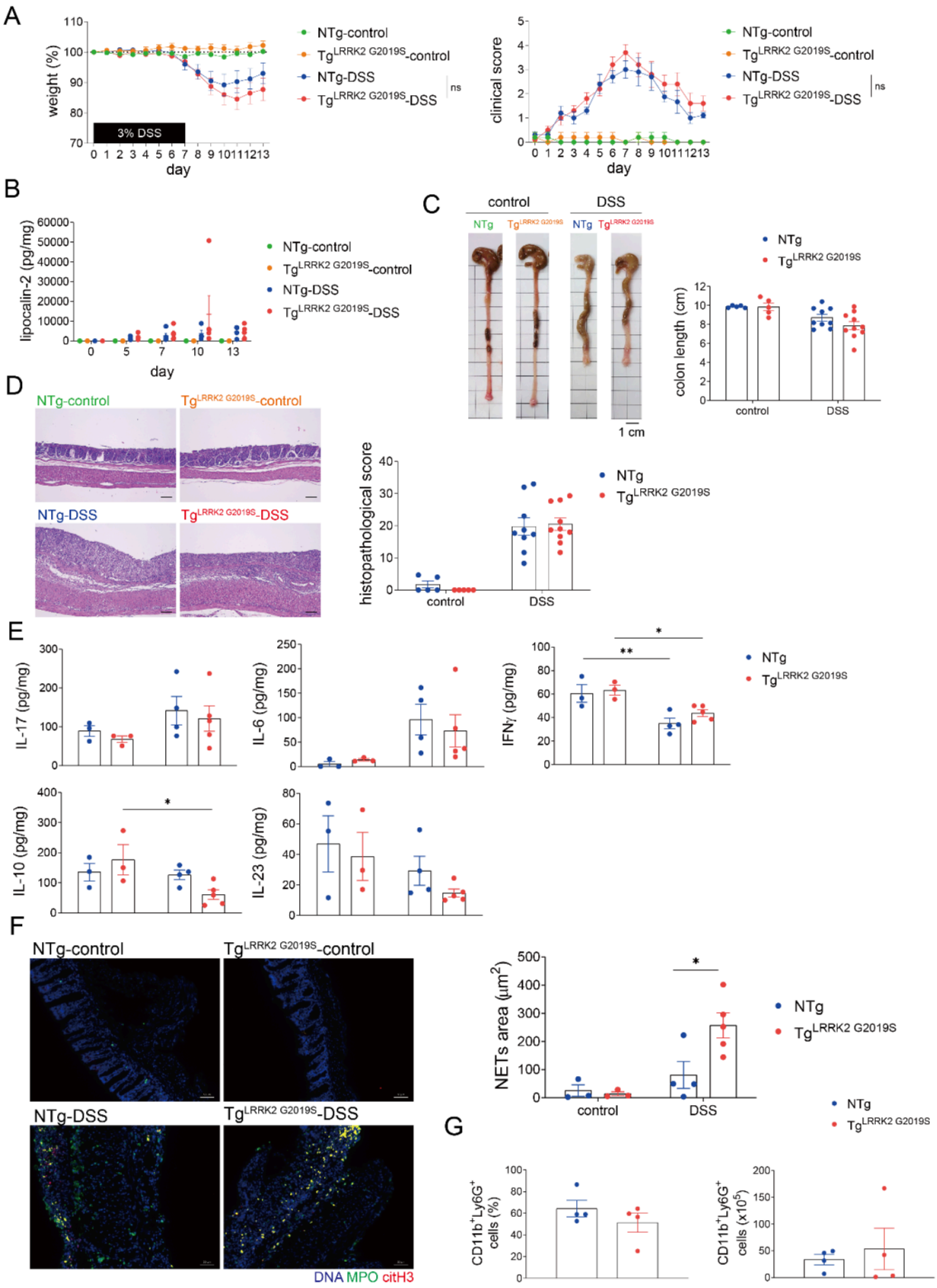


Figure 2

Enhanced NET formation precedes overt disease divergence during acute DSS colitis

A–B Weight change and clinical scores (**A**) and fecal lipocalin-2 levels (**B**) during DSS treatment. **C–F** Representative colon images and colon length quantification (**C**), representative H&E images of distal colon and histopathology quantification (**D**), selected colonic cytokine levels (**E**), and representative

immunofluorescence images and quantification of colonic NETs (**F**) after DSS treatment. **G** Percentage and number of neutrophils ($CD45^+CD11b^+Ly6G^+$) in the colonic lamina propria of DSS-treated mice. Data are presented as mean ± SEM. Scale bars, 100 μm in panel **D** and 50 μm in panel **F**. N = 3–5 for control groups and N = 4–10 for DSS groups in panels **A–E**; N = 4 for each group in panel **G**. *$P < 0.05$; **$P < 0.01$.

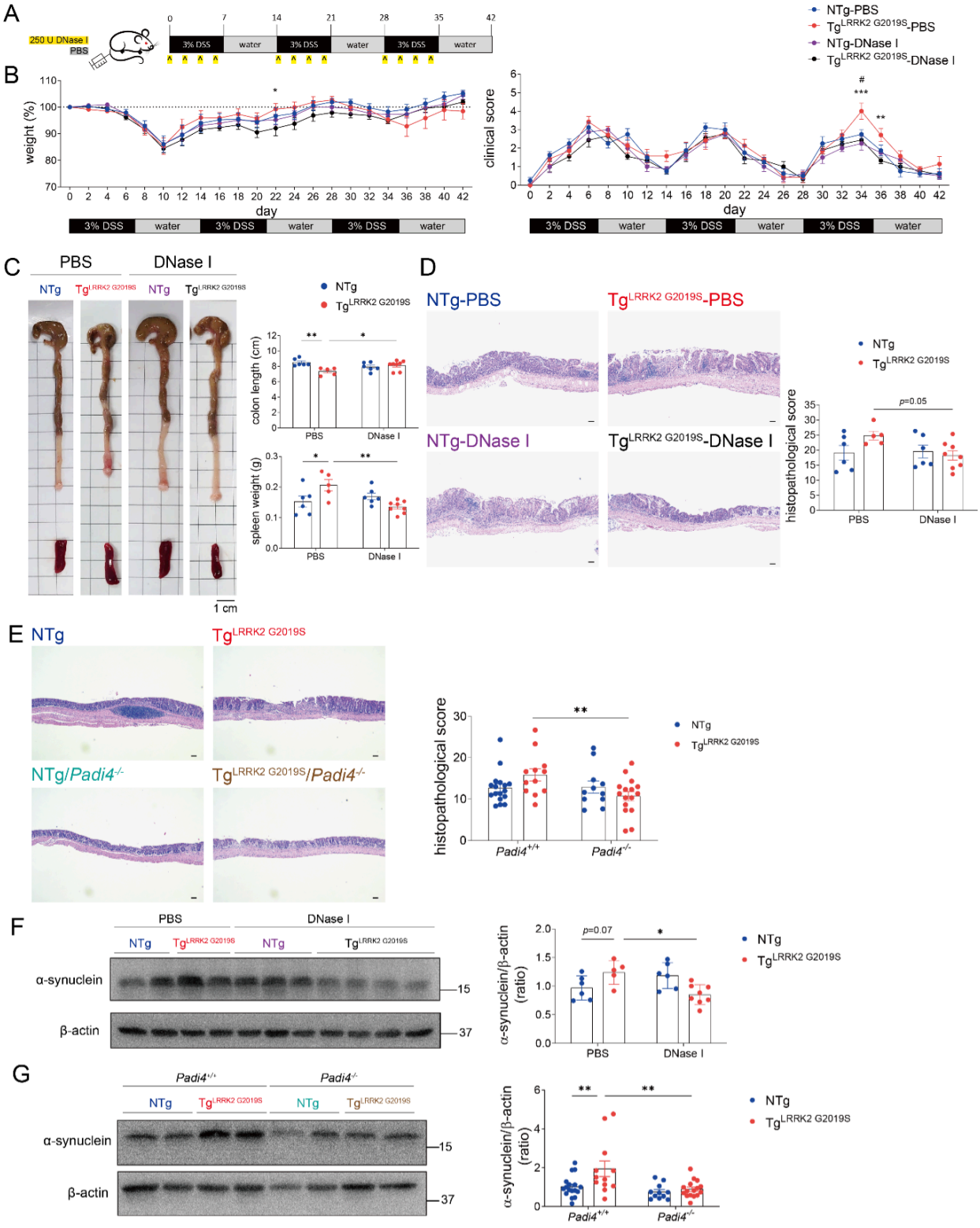


Figure 3

NET targeting partially ameliorates inflammation and reduces enteric α-synuclein accumulation in LRRK2 G2019S mice

A Experimental design. **B–D** Weight change and clinical scores (**B**) during repeated DSS treatment. Representative colon images and colon length quantification (**C**), and representative H&E images of distal colon and histopathology quantification (**D**) at the end of the experiment. **E** Representative immunoblots and quantification of α-synuclein in the distal colon of mice injected with or without DNase I after repeated DSS treatment. **F–G** Representative H&E images of the distal colon and histopathological scores (**F**), and representative immunoblots and quantification of α-synuclein in the distal colon of mice (**G**) with or without PAD4 deficiency after repeated DSS treatment. Data are presented as mean ± SEM. Scale bars, 100 and 50 μm in panel **D** and **F**. N = 7–8 for PBS groups and N = 8–10 for DNase I groups in panels **A** and **B**; N = 5–6 for PBS groups and N = 6–8 for DNase I groups in panels **C** and **D**; N = 12–17 for *Padi4*$^{+/+}$ groups and N = 11–16 for *Padi4*$^{-/-}$ groups in panel **F** and **G**. * and #, $P < 0.05$; ** $P < 0.01$; *** $P < 0.001$. In panel **B**, * indicates a significant difference between LRRK2 G2019S mice treated with DNase I and PBS; # indicates a significant difference between PBS-treated LRRK2 G2019S and NTg mice.

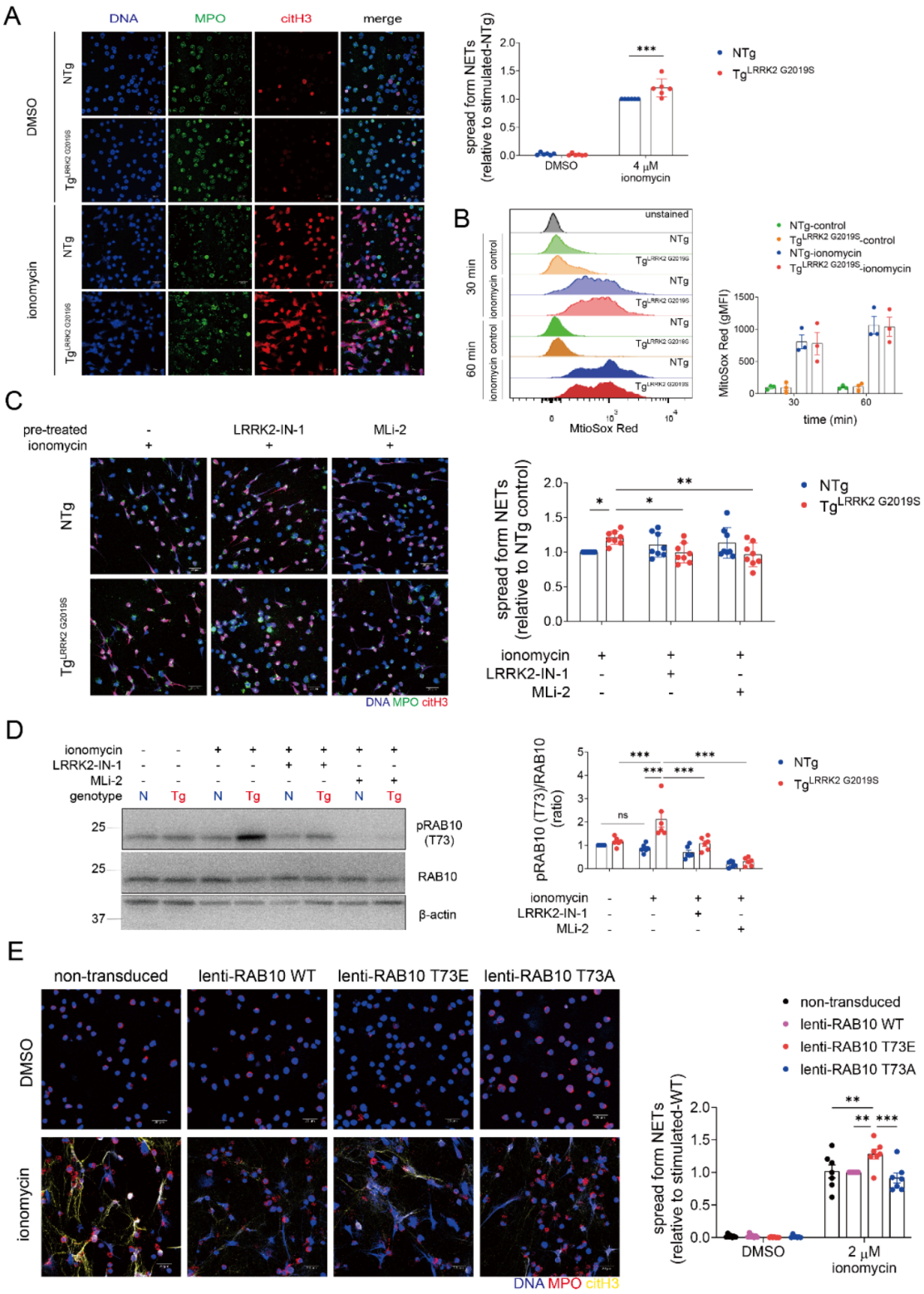


Figure 4

LRRK2 G2019S promotes NET formation in association with kinase-dependent RAB10 phosphorylation

A–B Representative immunofluorescence images and quantification of NETs released from NTg and LRRK2 G2019S neutrophils after ionomycin stimulation (**A**), and mitochondrial ROS levels in these neutrophils after ionomycin stimulation (**B**). **C** Representative immunofluorescence images and

quantification of NETs released from neutrophils pretreated with LRRK2 kinase inhibitors (0.5 μM LRRK2-IN-1 or 100 nM MLi-2) before ionomycin stimulation; percentages of NETs were normalized to ionomycin-stimulated NTg neutrophils without inhibitors, N = 8. **D**Representative immunoblots and quantification of phospho-RAB10 (T73; pRAB10) and total RAB10 in neutrophils treated with or without LRRK2 kinase inhibitors and stimulated with ionomycin for 3 h; pRAB10/RAB10 ratios were normalized to values from unstimulated NTg neutrophils in each experiment, N = 6. **E** Representative immunofluorescence images and quantification of NETs released from differentiated HL-60 (dHL-60) cells expressing mutant RAB10 after stimulation with 2 μM ionomycin for 3 h; percentages of NETs were normalized to ionomycin-stimulated lenti-RAB10 WT-expressing HL-60 cells, N = 7. Data are presented as mean ± SEM. Scale bars, 20 μm in panels **A**, **C**, and **E**. N = 6 in panel **A**; N = 3 in panel **B**. **P* < 0.05; ***P* < 0.01; ****P* < 0.001. ns, not significant.

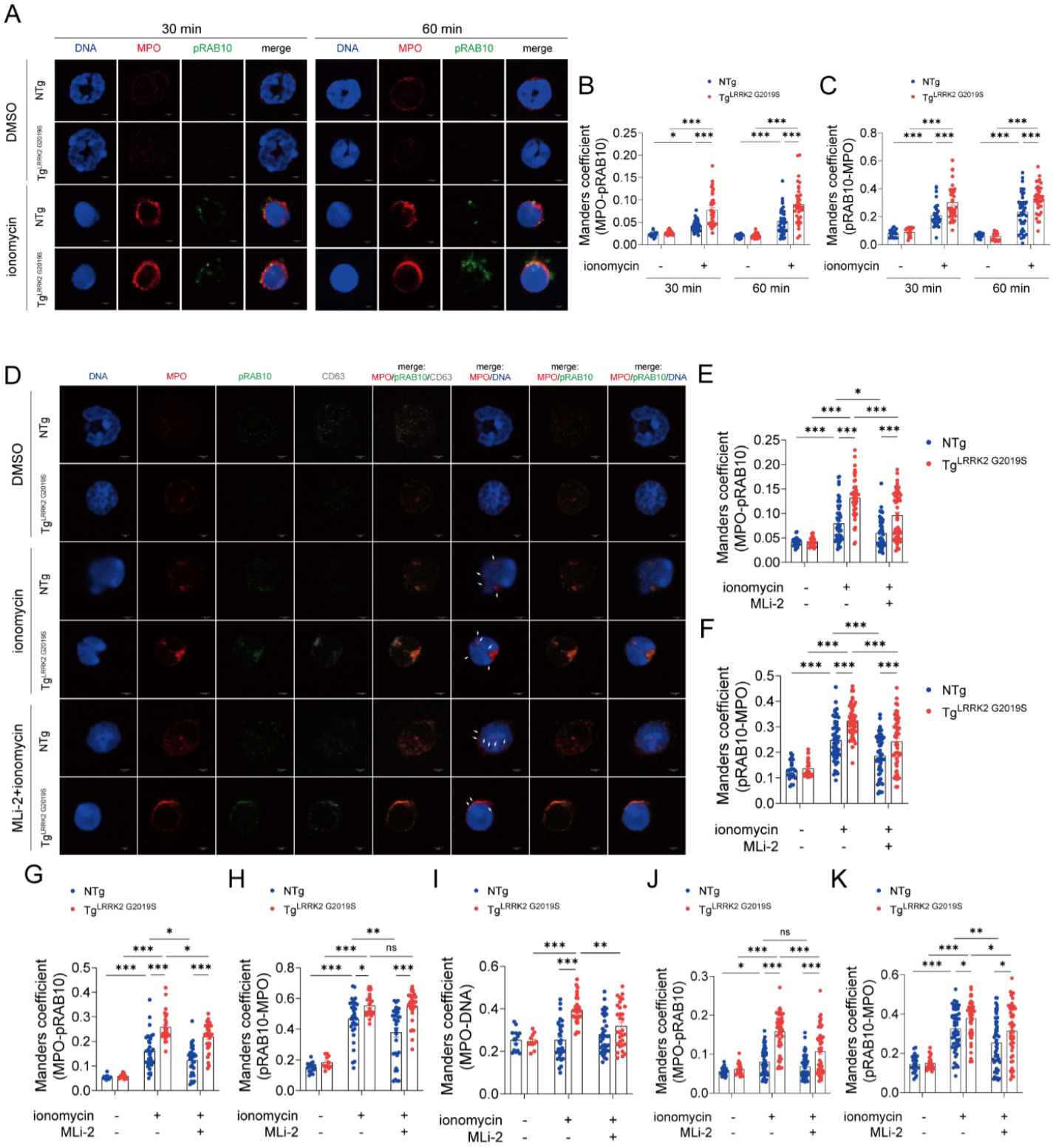


Figure 5

LRRK2 G2019S promotes pRAB10–MPO co-occurrence and MPO redistribution toward DNA^{+} regions in neutrophils

A Representative immunofluorescence images of NTg and LRRK2 G2019S neutrophils stimulated with or without ionomycin for 30 or 60 min. **B–C** Manders' colocalization coefficients for MPO with pRAB10 (**B**)

and pRAB10 with MPO at the indicated time points (**C**). **D** Representative immunofluorescence images of neutrophils pretreated with or without 100 nM MLi-2 followed by ionomycin stimulation for 60 min. White arrows indicate regions of MPO–DNA co-occurrence. **E–F** Manders' colocalization coefficients for MPO with pRAB10 (**E**) and pRAB10 with MPO (**F**) in whole cell. **G–H** Manders' colocalization coefficients for MPO with pRAB10 (**G**) and pRAB10 with MPO (**H**) within $CD63^+$ regions. **I** Manders' colocalization coefficients for MPO with DNA. **J–K** Manders' colocalization coefficients for MPO with pRAB10 (**J**) and pRAB10 with MPO (**K**) within DNA^+ regions of ionomycin-stimulated neutrophils treated with or without MLi-2. Data are presented as mean ± SEM. Scale bars, 2 μm in panel **A** and **D**. For panel **B–C**, 21–27 cells were analyzed in unstimulated groups and 35–40 cells in ionomycin-stimulated groups. For panel **E–F, J–K**, 21–24 cells were analyzed in unstimulated groups, 51–54 cells in ionomycin-stimulated groups, and 54–55 cells in MLi-2 plus ionomycin-treated groups. For panel **G–I**, 12–14 cells were analyzed in unstimulated groups, 29–31 cells in ionomycin-stimulated groups, and 33–35 cells in MLi-2 plus ionomycin-treated groups. N = 2–4 mice. *P < 0.05; **P < 0.01; ***P < 0.001. ns, not significant.

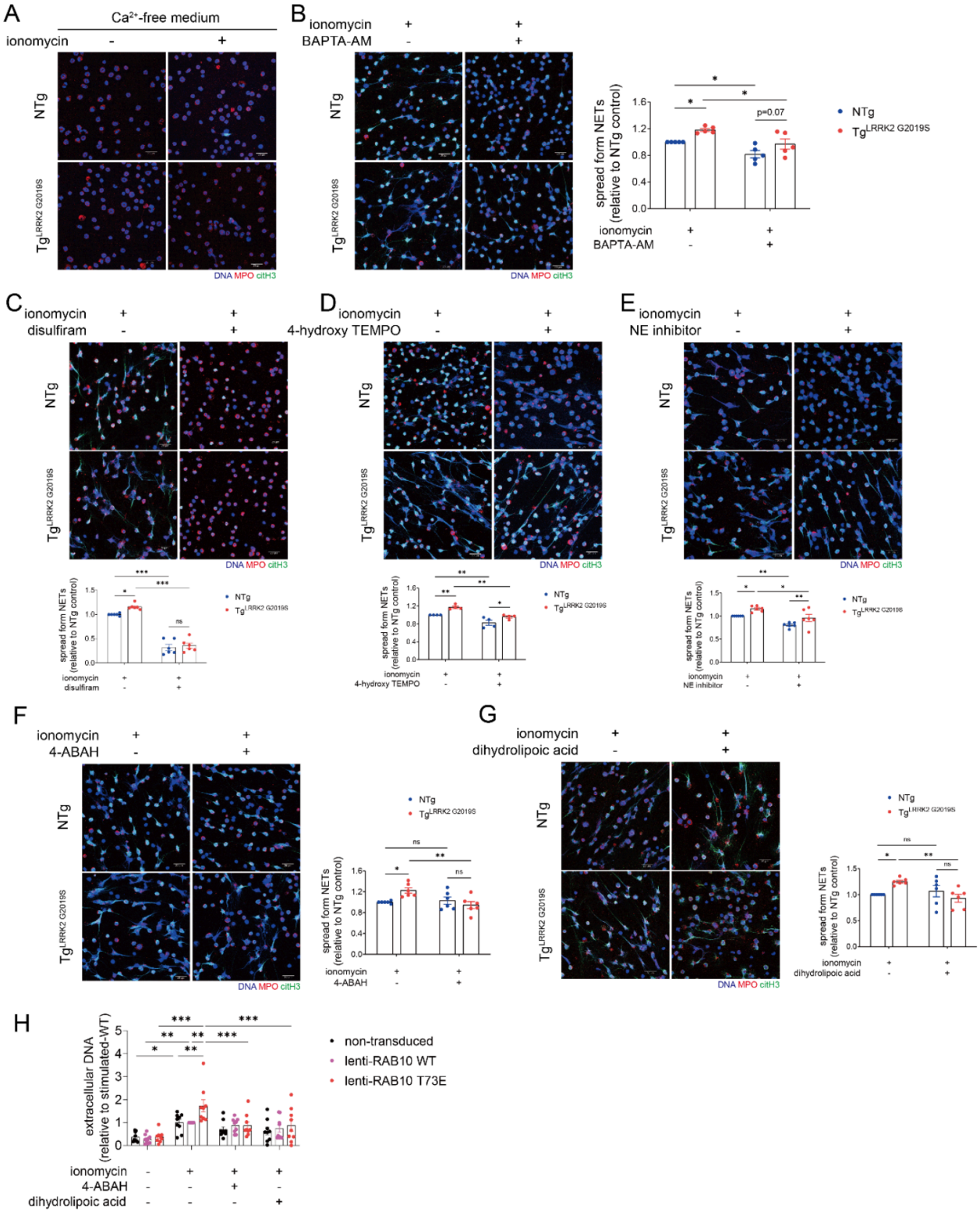


Figure 6

LRRK2 G2019S-driven NETosis requires MPO–HOCl signaling

A Representative immunofluorescence images of neutrophils stimulated with or without ionomycin in calcium-free medium. **B–G** Representative immunofluorescence images and quantification of NETs released from ionomycin-stimulated neutrophils treated with 100 μM BAPTA-AM (**B**), 10 μM disulfiram

(**C**), 100 μM 4-hydroxy-TEMPO (**D**), 50 μM NE inhibitor (**E**), 500 μM 4-ABAH (**F**), or 200 μM dihydrolipoic acid (**G**). **H** The levels of extracellular DNA released from 4 μM ionomycin-stimulated dHL-60 cells treated with 500 μM 4-ABAH or 200 μM dihydrolipoic acid. In panels **B–G**, percentages of NETs were normalized to ionomycin-stimulated NTg neutrophils without inhibitors. In panels **H**, percentages of extracellular DNA were normalized to ionomycin-stimulated lenti-RAB10 WT-expressing dHL-60 cells without inhibitors. Data are presented as mean ± SEM. Scale bars, 20 μm in panels **A–G**. N = 5 in panel **B**; N = 6 in panels **C**, **E**, **F**, and **G**; N = 4 in panel **D**; N = 9 in panel **H**. *$P < 0.05$; **$P < 0.01$; ***$P < 0.001$. ns, not significant.

Supplementary Files

This is a list of supplementary files associated with this preprint. Click to download.

- 20261119SupplementaryFigures.docx
- 20261119UncutBlotsCompressed.pdf